Cherenkov detector design for Hall D at Jefferson Lab

Conceptual design project report

Avanindra Joshi
Rensselaer Polytechnic Institute
Troy NY
2002

Table of Contents

Statement of the scope of the project and summary

The Cherenkov detector in the Hall D experiment at Jefferson labs is designed to be a C_4F_{10} gas-filled detector running at atmospheric pressure. It is intended to differentiate between energetic pions and kaons when time-of-flight measurements are unable to do so.

The objective of this project was to design and test the Cherenkov detector. An optical and mechanical design was achieved from computer simulations and physical tests. The dimension design of the optical mirrors was done using numerical simulations. Manufacturability and consistency of the manufacturing technique was physically tested. Photomultiplier tubes were selected based on this design. The shielding required for these PMTs were designed and tested using information from the overall design of Hall D. Finally, a solid model of the entire detector was built to facilitate visualization, integration with the overall Hall D design, and to facilitate further design modifications and analyses.

1. Introduction

The Continuous Electron Beam Accelerator Facility (CEBAF) at Jefferson Lab has proved immensely useful in evolving the presently understood picture of the behavior of strongly interacting matter. The important new experimental questions that these advances have revealed can be addressed by CEBAF at higher energies. Raising the energy of the accelerator to about 12 GeV, from the current 6 GeV provides several advantages. At such energies, the threshold above which the origins of quark confinement can be studied is crossed. Such energies also allow the direct exploration of quark-gluon structure of hadrons.

The addition of a fourth experimental hall, Hall D to the existing experiments at CEBAF is seen as a necessary step in probing these questions. The purpose of the Hall D experiment is to search for the so-called gluonic mesons with masses up to 2.5 GeV/c^2. To identify such states, the mechanism by which they are produced and their quantum numbers need to be known. Their decay modes also need to be understood and a high-resolution measurement of such modes with full acceptance is also necessary. The Hall D detector, therefore, must be able to measure the directions and energies of neutral particles and the momenta of charged particles with a 4π acceptance and high resolution. Reference 1 details more of the physics that motivates Hall D.

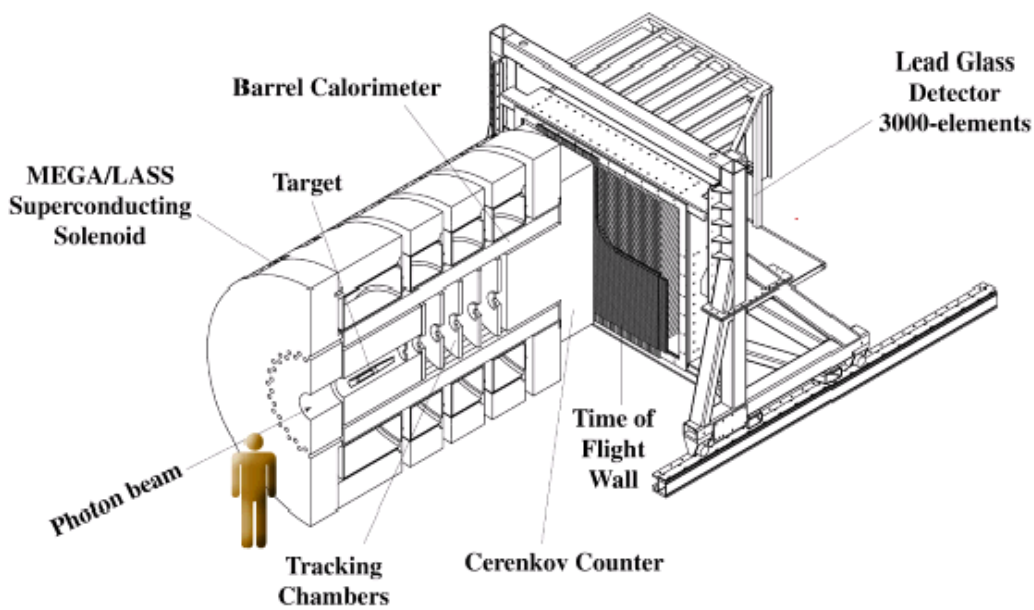

Figure 1 – Conceptual design of the Hall D experiment at Jefferson Lab

2. Design considerations and design objectives for the Cherenkov detector

Above 3 GeV, time-of-flight (TOF) measurements alone will not provide particle identification. The Cherenkov detector in Hall D will be used to identify high-energy pions when the TOF measurements cannot distinguish between pions and kaons. This Cherenkov detector is planned to be a gas-filled threshold detector running at atmospheric pressure.

The C_4F_{10} gas radiator with a refractive index, n = 1.00153 has been chosen for Hall D. This radiator has a threshold momentum of 2 GeV/c for pions and 9 GeV/c for kaons. The total physical volume space available for the Cherenkov in the proposed Hall D design is about 5 m x 5 m x 2 m.

The design objectives for the Cherenkov detector in the ambit of this project were:

1. Design, locate and orient ellipsoidal mirrors with reference to the target
2. Test mirrors for surface quality, curvature consistency and manufacturability
3. Numerical simulation to verify results and aid in design
4. Locate the photo-multiplier tubes and design shielding for the same
5. Solid modeling for manufacturing, testing and assembly

The basic design of the Cherenkov detector consists of a cylindrical box divided into sixteen azimuthal regions. Each region consists of two-mirror reflecting assembly and a PMT. The expected performance of this design is described in Reference 2.

3. Mirror Design

The functionality of the mirrors in the Cherenkov detector in Hall D is to focus the Cherenkov light originating at the target to the light-collecting and signal-generating devices, namely the PMTs. Ellipsoidal mirrors were chosen for this purpose to avail of the optical properties of ellipses that each of the two foci focus light on to the other.

A first order estimate of the size of each of the sixteen mirror segments was obtained by calculating the size of the 'virtual' target. The virtual size of the target is the diameter of the extended object that focuses on to the mirror considering the solenoidal magnetic field in the region of the target. The magnetic field has a magnitude of 1.8 Tesla. For particles with a momentum of 2.9 GeV/c, it was estimated that the radius of the target as seen from the front of the detector would be about 270 mm. This translates into the fact that the radial size of the ellipsoidal mirrors would have to be at least as much to accommodate an optical object of this extended size. It was decided that a radial size of 1000 mm us suitable for the ellipsoidal mirrors.

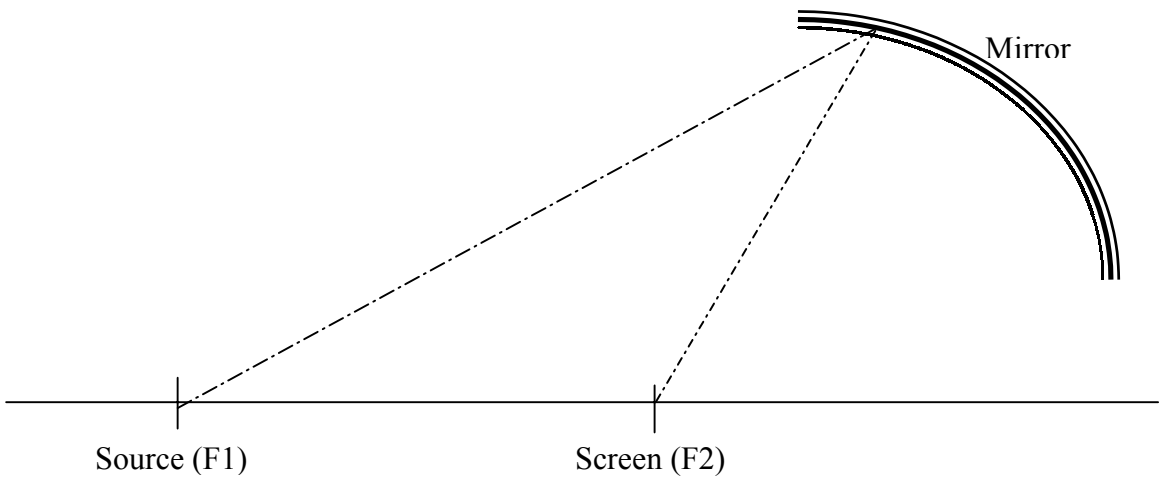

Figure 2 – Line diagram of the experiment setup to assess mirror properties indicating mirror, light source and screen

Since photons traverse the Cherenkov detector, a primary design constraint for the ellipsoidal mirrors of this type is that they need to be extremely low in mass. At the same time, they have to be flexible enough to allow for focusing adjustments. A construction and design method for very light mirrors with ellipsoidal curvature has been studied by Chan, as detailed in Reference 3 . Such mirrors must be rigid under cutting impacts and retain curvature upon being cut to conform to the desired shape. It is also required that these mirrors have a good surface quality and uniform reflectivity.

To assess whether these properties can be obtain using the mirror construction method under consideration, a series of tests were conducted. In these tests, the reflection properties of prototype mirrors were documented using a point light source. The point light source was given small displacements to understand reflection properties as a function of surface quality as well as overall curvature consistency. Finally, the mirrors were cut using a power saw and the same tests performed to determine of they retained curvature after mechanical cutting.

The prototype mirrors used in these tests were EL-12, EL-19 and EL-20, Reference 3. These were constructed in 1995 as part of the design of the C8 Cherenkov detector in the E852 experiment at Brookhaven National Labs. These mirrors were assembled from carbon fiber/epoxy layers surrounding a vinyl foam core. A simple line diagram indicating the geometry of these tests is in shown in Figure 2. Table 1 presents the details of these tests and the results obtained.

Single-stage versus double-stage reflection

Based on calculations of virtual target size and preliminary assessments of the mirror sizes, the position and orientation of the PMTs was estimated. These calculations indicated that the second focus of these ellipsoidal mirrors which coincides with the PMT would have to be in a region of very high magnetic field. Alternatively, if the mirror curvature was adjusted to focus a larger distance away to avoid this problem, there was a dramatic increase in linear magnification. Several permutations and combinations later, this problem was resolved by having a two-stage reflection assembly that finally focuses on to the PMTs.

No	Test	Results	Remarks
1	Test to determine Spot Size	30 mm x 20 mm	The PMT diameter should be greater than this. A 2 inch PMT suits this data
2	Test to determine curvature consistency		
	The source was moved along the beam axis to account for the finite (300 mm size of the target)	F2 moves by about 55 mm x 160 mm	The mirror curvatures are not consistent
			The PMT needs to be big enough to accept the 160 mm swing
3	Test to determine surface quality		
	A laser beam was traversed along the length of the mirrors and the "jump" in the spot size was measured	"Jump" of about 35 mm x 7 mm	
4	Test to determine curvature retention on cutting		
	The mirror was cut using a saw and the same tests performed on other samples	Results from spot-size test, etc. were similar to above	The manufacturing technique used for these mirrors is robust enough to retain curvature and surface properties after cutting
5	Test to compensate for curvature due to magnetic field	Effective target size was of 560 mm radius	The mirror size needs to be at least of this order

Table 1 – Details of the tests and results to assess mirror surface quality and manufacturability

4. Numerical simulations

With the objective of obtaining refined designs for the two-stage mirror and locating the two stages, a numerical simulation was used. All work described in this section was done in collaboration with Jane Krenkel and Gary Adams. The inputs to this simulation were events with median pion energy of 2.5 to 3 GeV as described in Reference 4. As a part of this simulation were plotted the detection percentage of the detector. The data obtained from this simulation for first stage mirrors is presented in Figure 3. Figure 3 (a) shows the front view as seen from the target and Figure 3 (b) shows the side view of the first stage mirror. The unit of length on the axes for both the figures is in centimeters.

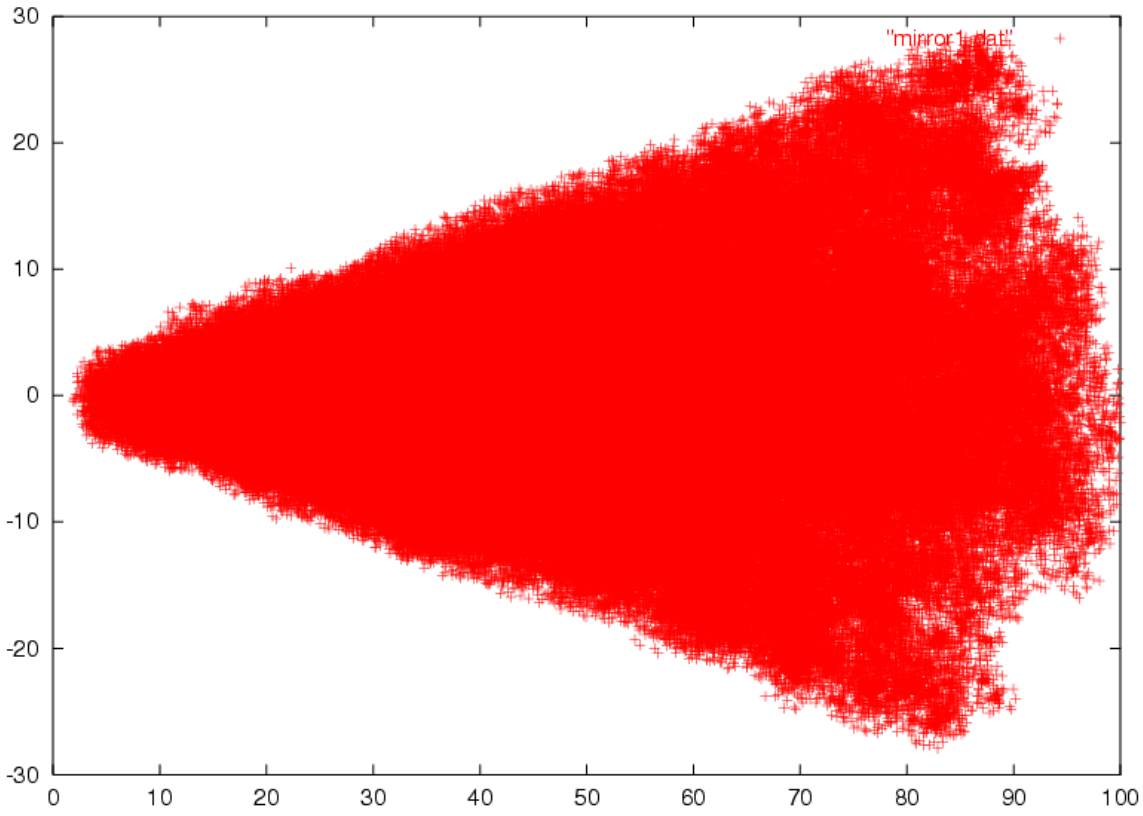

Figure 3 (a) – Front view of the first stage mirrors as generated using the Monte-Carlo simulation

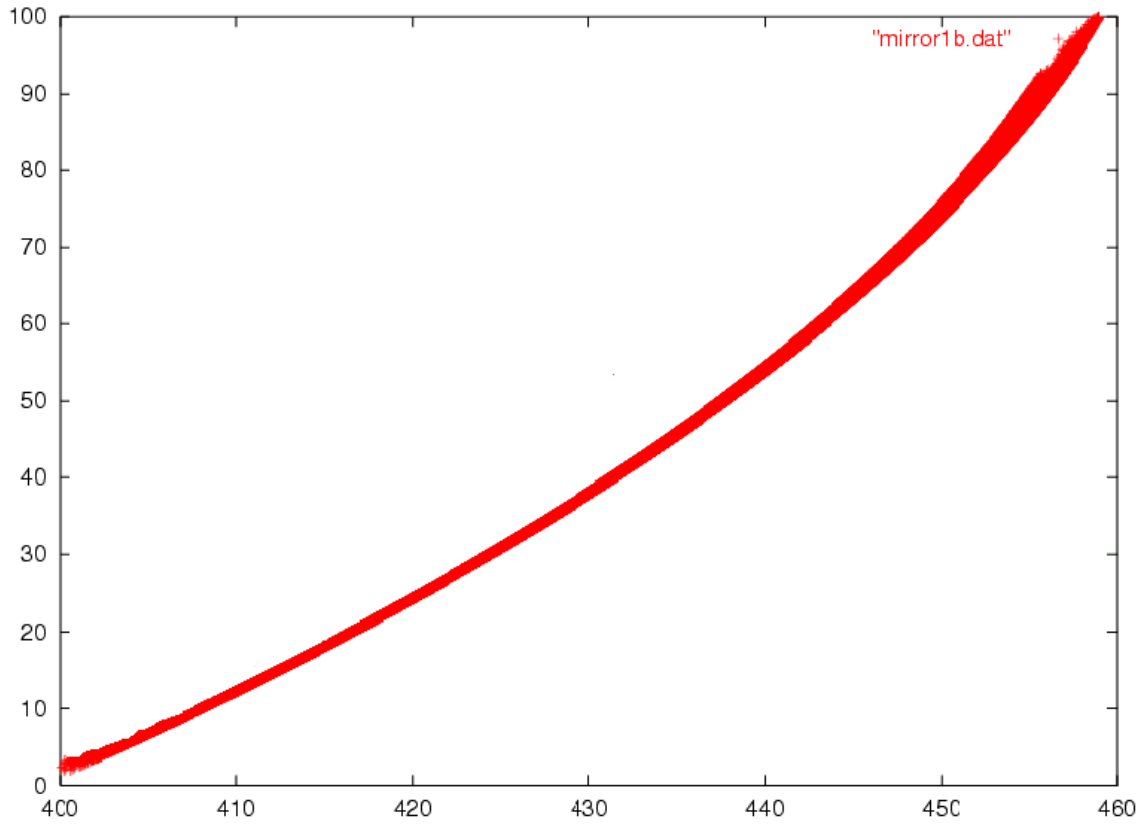

Figure 3 (b) – Side view of the first stage mirrors as generated using the Monte-Carlo simulation

The simulation served well to verify that the mirrors need to have a full width of about 600 mm at the maximum radial value of 1000 mm. The side-view results also indicate with a good accuracy the location of the ellipsoidal piece.

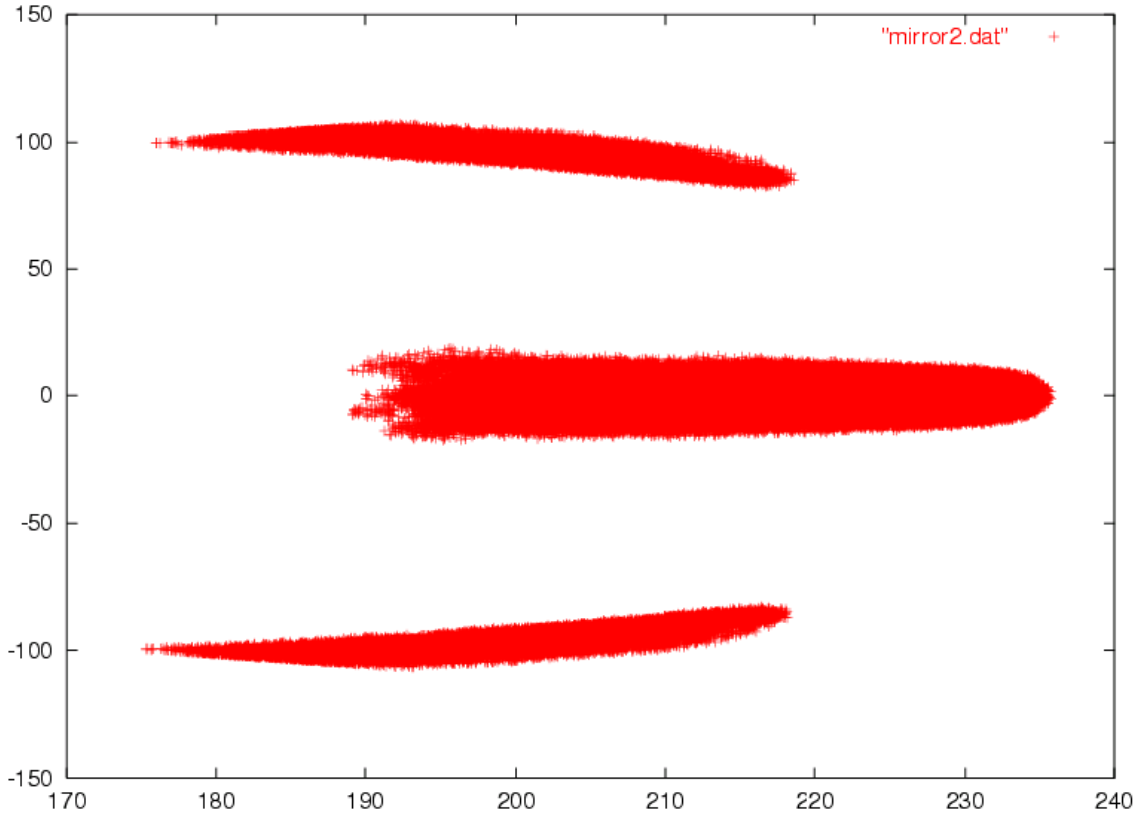

Figure 4 (a) – Front view of the second stage mirrors as generated using the Monte-Carlo simulation

Figure 4 (a) shows the front view of the second stage mirrors. The two auxiliary 'bands' of light from events in one azimuthal section are to be noted. They represent light that was generated by particles in one azimuthal section. Figure 4 (a) indicates that this light crosses over to the adjacent sections. This cross-over complicates the analysis of charged tracks. To minimize this, the second stage mirrors were designed to have a width that would only accommodate the central prominent band of light.

Figure 4 (b) shows the side view of the second stage mirrors. This view indicates the radial location of the mirrors above beam-axis. The axes for Figure 4 (a) and (b) are in centimeters. For both Figure 3 and Figure 4, the axes are based on a global frame of reference centered at the target.

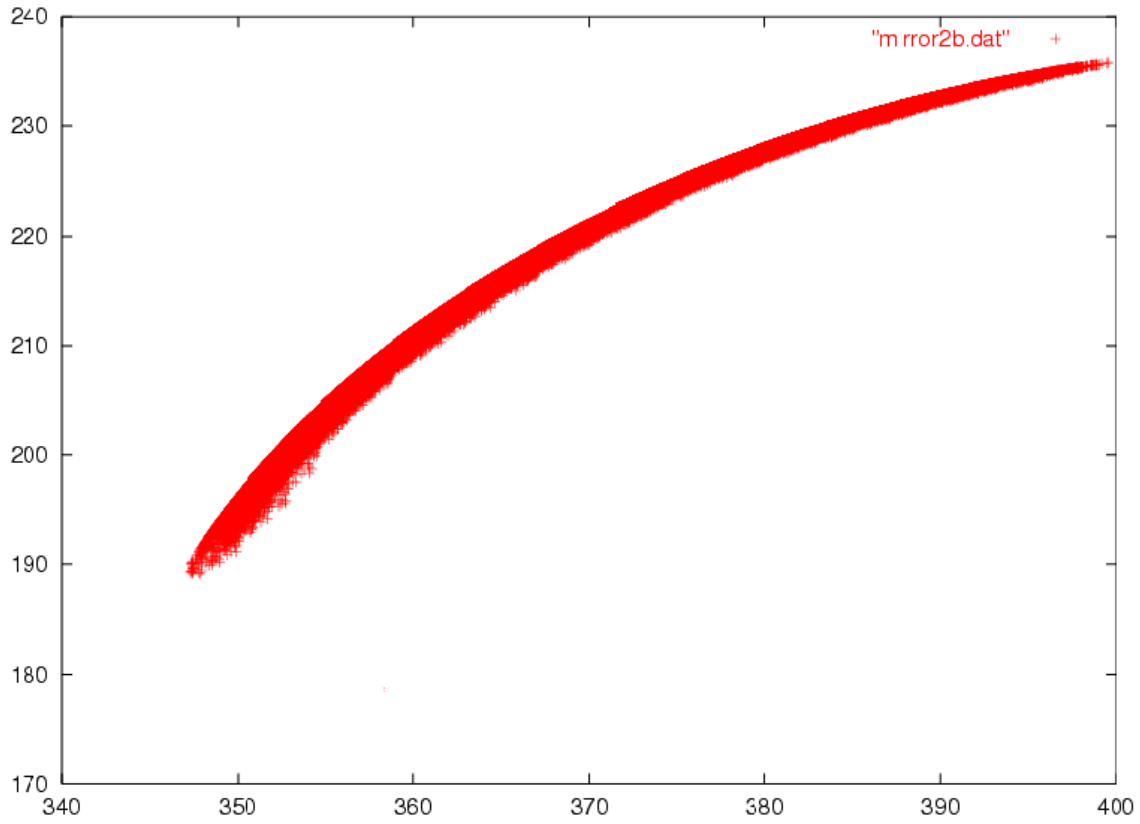

Figure 4 (b) – Side view of the second stage mirrors as generated using the Monte-Carlo simulation

The Monte-Carlo simulation served well to verify that events above the threshold are detected. It also helped determine accurate dimensions for the mirrors. The simulation also indicated with accuracy the positioning and location of the two mirror stages.

5. Determination of PMT size and design of the PMT shielding

Results from Table 1 and the simulation both indicated that a PMT of 5 inch (129 mm) diameter is necessary to collect the light using the proposed optical arrangement. The PMT model chosen was the 14-stage model number 8854 Quantacon PMT by Burle having a quantum efficiency of 22.5 % at 385 nm Reference 12. This PMT has a very high-gain first stage and is well suited to low-level light measurements.

Using the commercial magnetic elements design program flux2D, the shields were designed for the PMT. At the location of the PMT, the normal component of the magnetic field has a value of about 0.04 Tesla from the computations described in Reference 5. The geometry of the optics has been chosen such that the axial component of the applied magnetic field is negligible. Using standard-gauge Conetic and Netic materials, Reference 6, the shields were determined to have four layers, each of thickness 0.06 inches (1.52 mm). Table 2 lists the dimensions of the four layers of shielding.

Stage	Diameter	Shell Thickness	Length	Material
	dimensions in inches			
1	7.5	0.06	14.00794	NETIC
2	6.865079	0.06	13.13492	CONETIC
3	6.230159	0.06	12.57937	CONETIC
4	5.595238	0.06	11.26984	CONETIC

Table 2 – Details of the PMT shielding

Numerical simulation of the PMT shielding

To verify that the shielding designed as above is effective, numerical modeling and testing of the PMT shielding was deemed necessary. Figure 5 shows the results obtained from this simulation for flux lines using the magnetic component design program flux 2D (Reference 7). In this simulation, the saturation properties of the material were included. This 2-dimensional simulation predicts the field at the center of an infinitely long, cylindrically symmetric shielding assembly.

In order to account for the rate of fall of the field along the PMT axis, a 3-dimensional simulation was performed using the finite element code flux3D (Reference 7). The results from the 3-dimensional simulation were consistent with those from the 2-dimensional simulation.

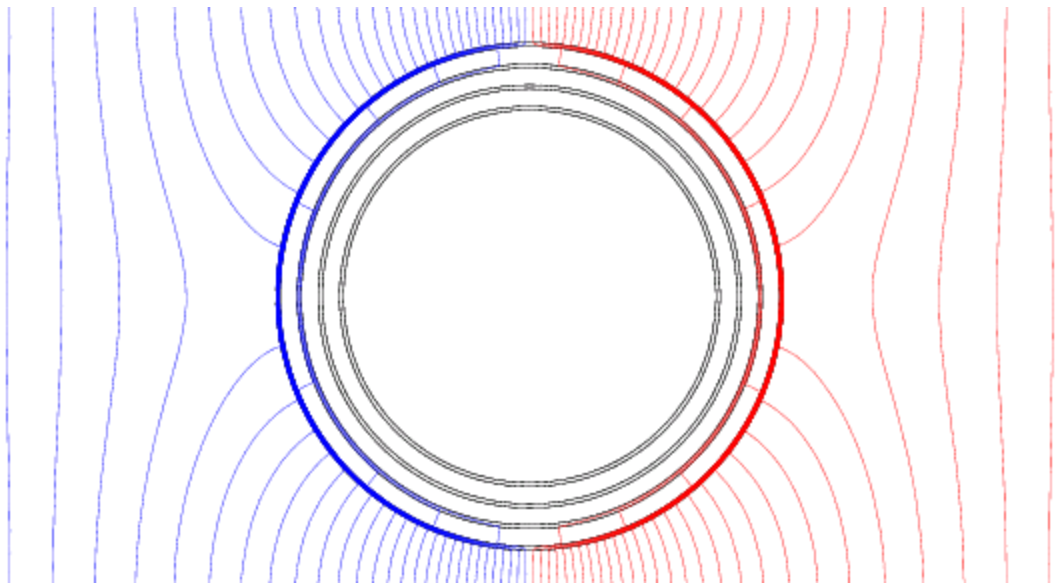

Figure 5 – Magnetic flux lines at PMT shielding

Figure 6 indicates the results for the normal component of the magnetic flux density obtained using the magnetic elements design program flux3D. The component of the magnetic flux density B normal to the cylindrical shielding is plotted against the axial length along the PMT axis. The reference frame is centered at the center of the cylindrical PMT. The result indicates how the Z –component falls off as a function of axial length.

The physical location of the PMT shielding is approximately between -8 cm and +8cm. The photocathode is located at -5 cm and the field at the photocathode is predicted to be 0.000018 Tesla. Outside this region, the field is of the order of 0.04 Tesla as expected. An internal field of 0.000018 Tesla is sufficiently small so that the PMT efficiency will not be affected. This shield geometry has been included in the solid-model design of the Cherenkov detector.

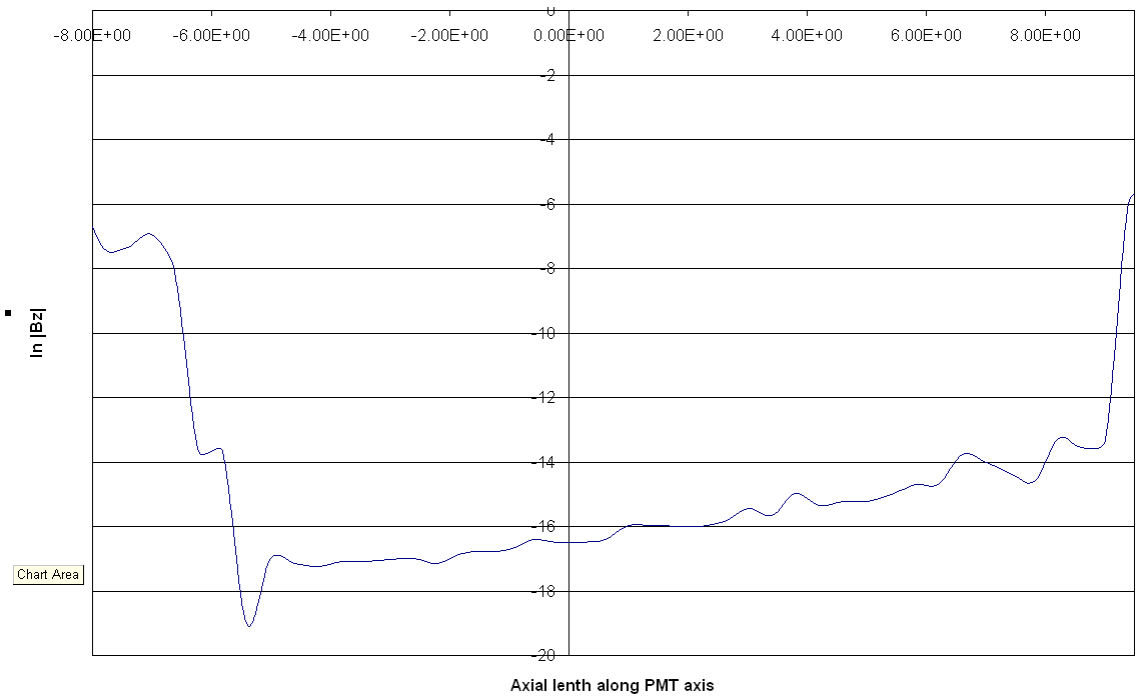

Figure 6 – Plot of the normal component of the magnetic flux density at the PMTs as a function of axial distance along the PMT axis

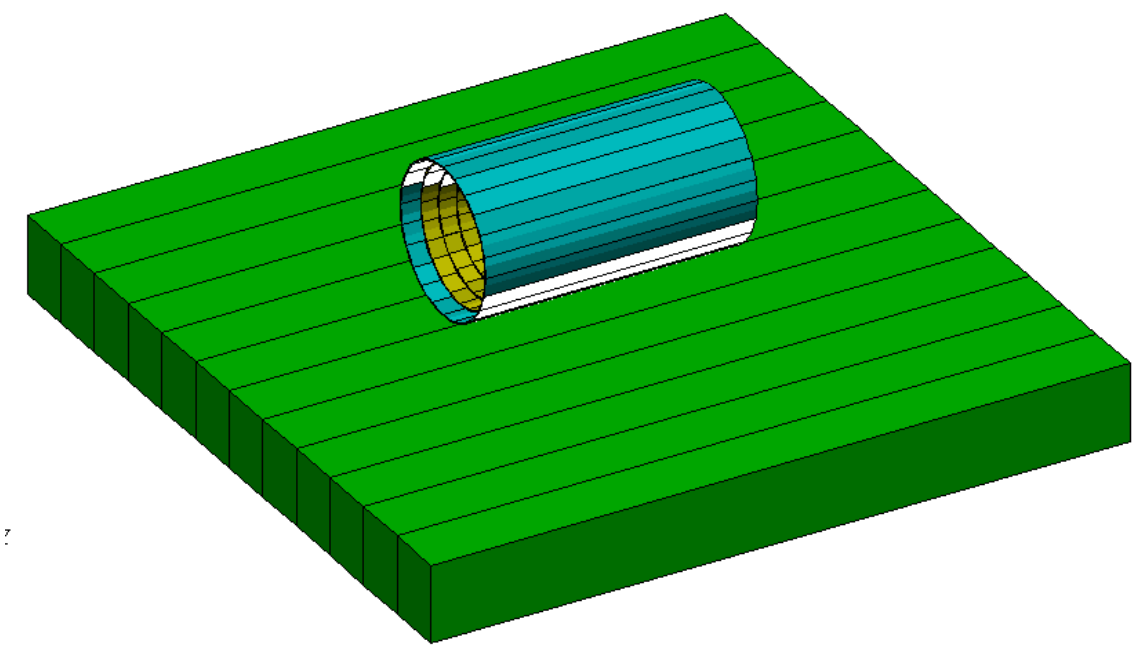

Figure 7 – Representative drawing of the test of magnetic shielding inside a large dipole of 0.04 Tesla. Note that only the lower pole is shown for clarity.

PMT shields testing

The PMT shields designed as above were prototyped to be tested. The assembly was placed in a large dipole magnet at Brookhaven National Lab to simulate a uniform magnetic field of strength 0.04 Tesla. Figure 7 shows the representative arrangement of this test. Only the lower pole of the dipole is shown for clarity. Measurements of the field density inside the shielding using Hall probes indicated that the rate of decrease of the normal component is not as rapid as desired.

This test was numerically modeled to be sure that the test geometry was not at fault. Shielding factors comparable to the ones described above were achieved. Therefore, it is unlikely that the use of a dipole magnet in the test significantly affected the results. Instability in the Hall probe outputs made the results inconclusive. More test of the magnetic shields are needed.

6. Solid Modeling of the design

For the purposes of visualization and design verification, the entire Cherenkov detector assembly was modeled using the solid-modeler I-DEAS. The choice of solid modeling software was based on integration with overall Hall D design and the ease of FE testing.

Figure 8 shows the side view of the final solid model of the Cherenkov detector for Hall D. Only the optical components are included. The green arrow indicates the beam. The relative positions of the optical elements are in the true geometric orientation. The first stage mirrors are colored red, the second stage mirrors are yellow and the PMTs and shielding are blue.

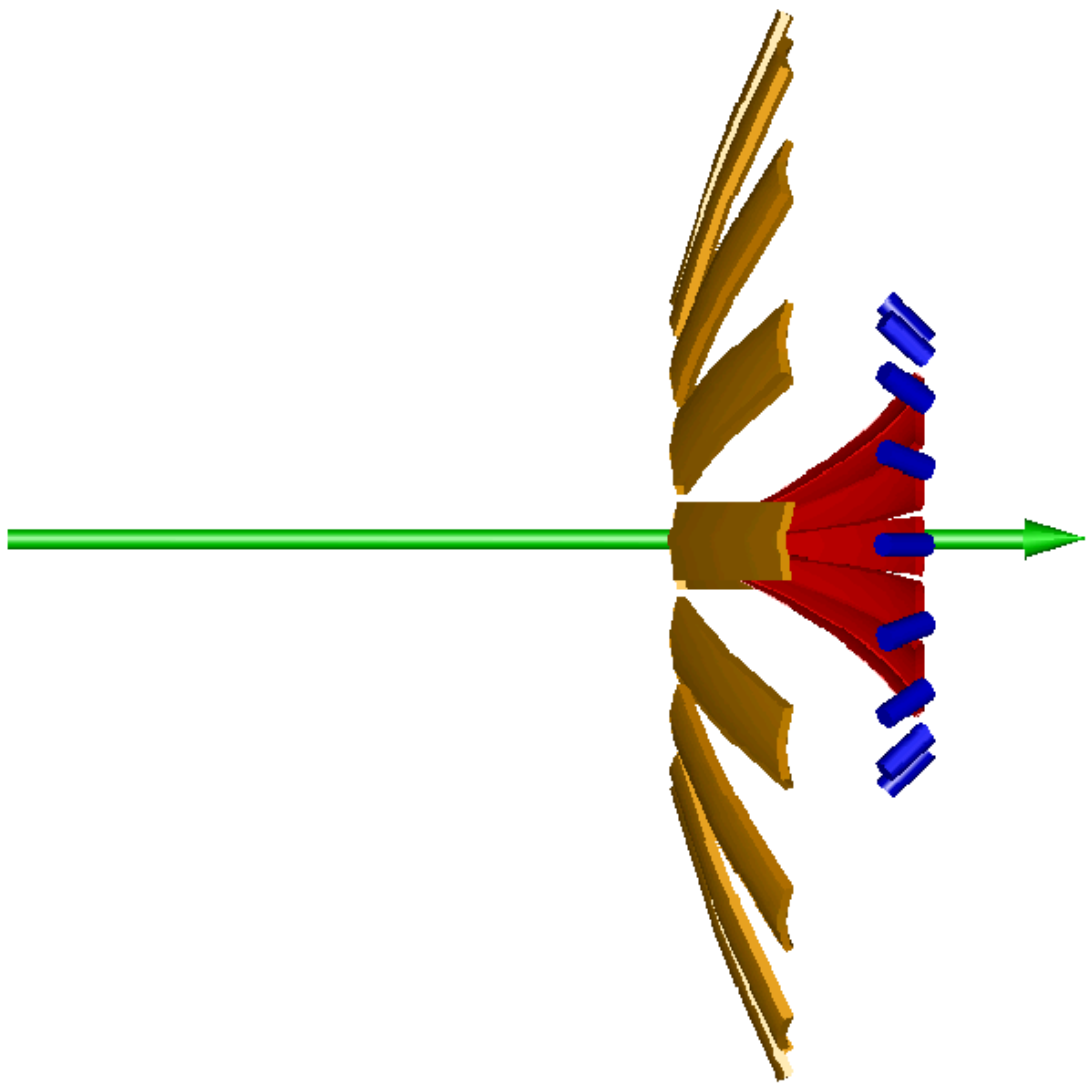

Figure 8 – Side view of the optical elements of the final design for the Cherenkov detector for Hall D

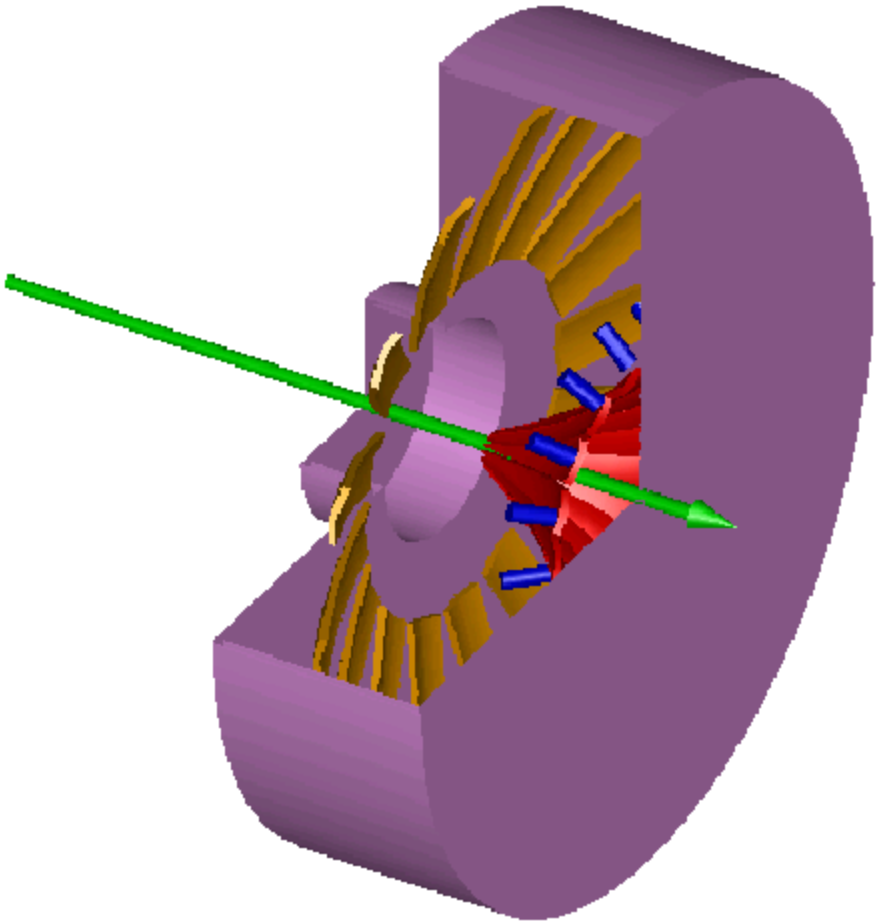

Figure 9 – Isometric view of the final design of the Cherenkov detector for Hall D

Figure 9 shows the isometric view of the final design. A stage-wise view of the four-stage PMT shielding is obscured by the scale of the figure. The cutaway cylindrical box is the outer gas container whose outer diameter is estimated to be around 5000 mm.

References

1. http://dustbunny.physics.indiana.edu/HallD/Overview.html
2. Adams G, Heinz R; “Status of the PID System”, Hall D note no. 48 [2001]
3. Chan Y-W; “Detail design and construction of the optical section of the Cherenkov detector”, MS Thesis, RPI [1995]
4. Bellis M, Adams G & Cummings J; “"PID acceptance using TOF, Cherenkov Counters and Kinematic Fitting", Hal D note no. 38 [2000]
5. Adams G; "Magnetic Field Calculations", Hall D note no. 42 [2000]
6. Magnetic Shield Corp., 740 N Thomas Drive, IL 60106
7. Magsoft Corp., 1223 Peoples Ave. Troy NY 12180
8. The science driving the 12 GeV upgrade of CEBAF, Jefferson Lab 2001
9. Shielding design of Hall D LGD, Lu Minghui, March 2001
10. Cherenkov Detector Progress Report, Adams G, Joshi A, Krenkle J, Sept 2001
11. Experimental Techniques in high-energy physics, Ferbel T
12. Burle Co., 1000 New Holland Ave. Lancaster PA 17601, Photomultiplier 8854 data sheet

Appendix – Hall D Notes

PID Acceptance Using TOF, Cerenkov, and Kinematic Fitting

M. Bellis, G. Adams, and J. Cummings
Rensselaer Polytechnic Institute
7/10/00

The HDFAST monte carlo code was used to estimate the acceptance of the Hall D spectrometer for the reaction $\gamma p \rightarrow Mp \rightarrow K^*K^*p \rightarrow K^+K^-\pi^+\pi^-p$ with a 9 GeV photon beam. All events were for a single resonance, M, with a mass of 2.0 GeV and width of 300 MeV, as in the previous simulations. The goal of this study was to determine if kinematic fitting of kaon events would compensate sufficiently for incomplete particle identification to allow one to determine exclusive events with large acceptance. Two atmospheric-pressure Cerenkov detectors were considered, one with an aerogel radiator (n=1.008) and one with C_4F_{10} gas.

Three detector systems were included in the simulation, time-of-flight from the barrel calorimeter (sigma = 250 ps), time-of-flight from the downstream hodoscope (sigma = 80 ps), and threshold momenta for the Cerenkov detector. Proton identification was assumed to be 100 percent efficient. Smeared flight times, momenta and path lengths were used in the calculations (see Fig.1). With the exception of the Cerenkov detector, the geometry of all elements was determined by HDFAST. An additional dead region near the beam was incorporated into the Cerenkov detector. Tracks hitting the detector within 10cm of the beam were not counted.

The tof acceptance for charged tracks was determined by flagging events for which the calculated difference in tof between a pion and kaon of equal momenta was less than three times the resolution of the detector. This three-sigma limit will suppress pion contamination in the kaon signal by about a factor of 25. Three different values were tried for the resolution of the downstream hodoscope: 70, 80, and 90 ps.

The Cerenkov detector was incorporated with sharp thresholds for pion and kaon identification. Since the precise response of the detector is not yet known, the threshold was incorporated at a fixed spacing (100 MeV/c) above the calculated threshold for each particle type to emit Cerenkov light. This produces a momentum window for each radiator for which the detector can identify kaons. The aerogel radiator functions between 1.2 and 4.0 GeV/c, and the gas discriminates at a higher range, 2.8 to 10.0 GeV/c. Table 1 summarizes the detector response when the hodoscope resolution was set to 80 ps.

Table 1: Fraction of events with N ambiguous hits, in percent.

	N=0	N=1	N=2	N=3	N=4
aerogel	15	39	33	11	1
gas	26	43	25	5	1

The results indicate that neither Cerenkov radiator is able to unambiguously identify a large fraction of the events. In principle those events with only one ambiguous meson can be recovered by requiring strangeness conservation. The price one pays is an increased sensitivity to pion contamination. In this report we consider a second approach; events with ambiguous hits were fitted to all available hypotheses and the best fit was chosen. Using this in conjunction with strangeness conservation should yield high acceptance and good background rejection.

The 3-momenta of all tracks were varied in the fit, with constraints provided by energy and momentum conservation. The error matrix from HDFAST was used for each track. For those events having two ambiguous hits, only hypotheses consistent with

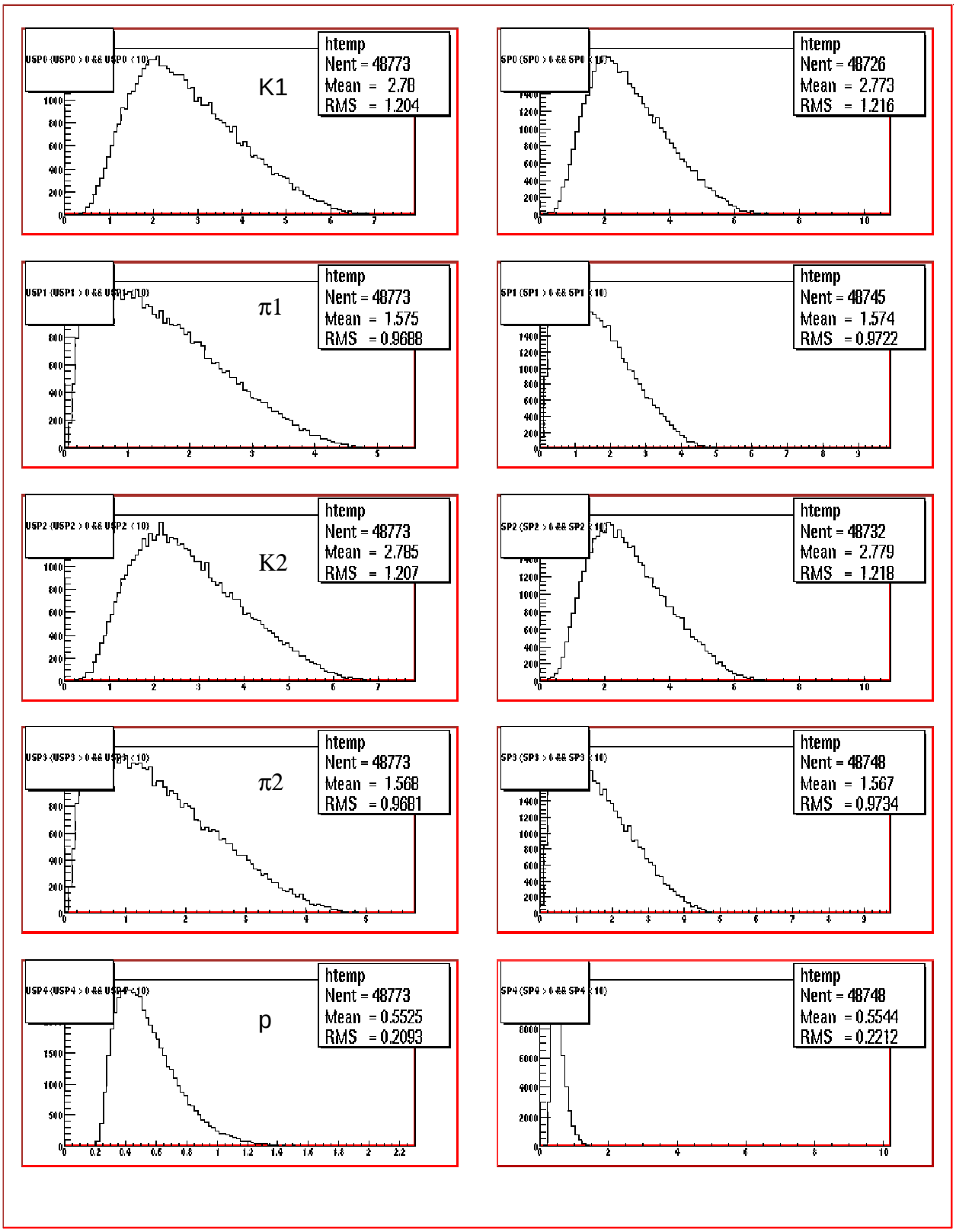

Fig. 1 - Unsmeared (left) and smeared (right) momentum distributions.

strangeness conservation were tested. Table 2 shows the fraction of events that was correctly identified by the kinematic fitting test. These results show that kinematic fitting

Table 2: Acceptance (in percent) when events with N ambiguous hits are fitted.

	N=0	N=0+1	N=0+1+2
aerogel	15	52	83
gas	26	66	88

is an effective method for extending the range of either Cerenkov radiator. The largest losses came from events where one pion and one kaon were ambiguous before the fit. Fig. 2 characterizes the events that were missidentified. The variation of acceptance with TOF resolution is shown in Fig. 3.

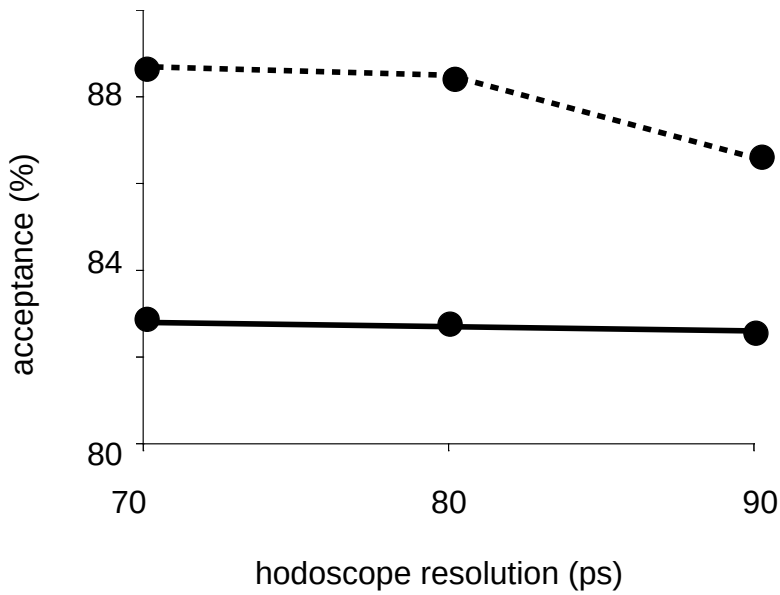

Fig. 3 - PID acceptance for hodoscope resolution equal to 70, 80, or 90 ps.

Studies are now underway to determine the PID acceptance for a reaction with fewer particles, $\gamma p \rightarrow Mp \rightarrow K^{*}Kp \rightarrow K^{+}K^{-}\pi^{0}p \rightarrow K^{+}K^{-}\gamma\gamma p$. This reaction necessitates the use of the LGD in the kinematic fit and hence may result in lower resolution for particle mass. Also, with only three mesons in the final state one can anticipate that the average momenum of each particle will be shifted higher than for the present case, resulting in a larger difference between the gas and aerogel acceptances. This consideration and the fact that the gas results in a slightly higher acceptance (Table 2) leads us to conclude that a gas Cerenkov is favored over an aerogel radiator.

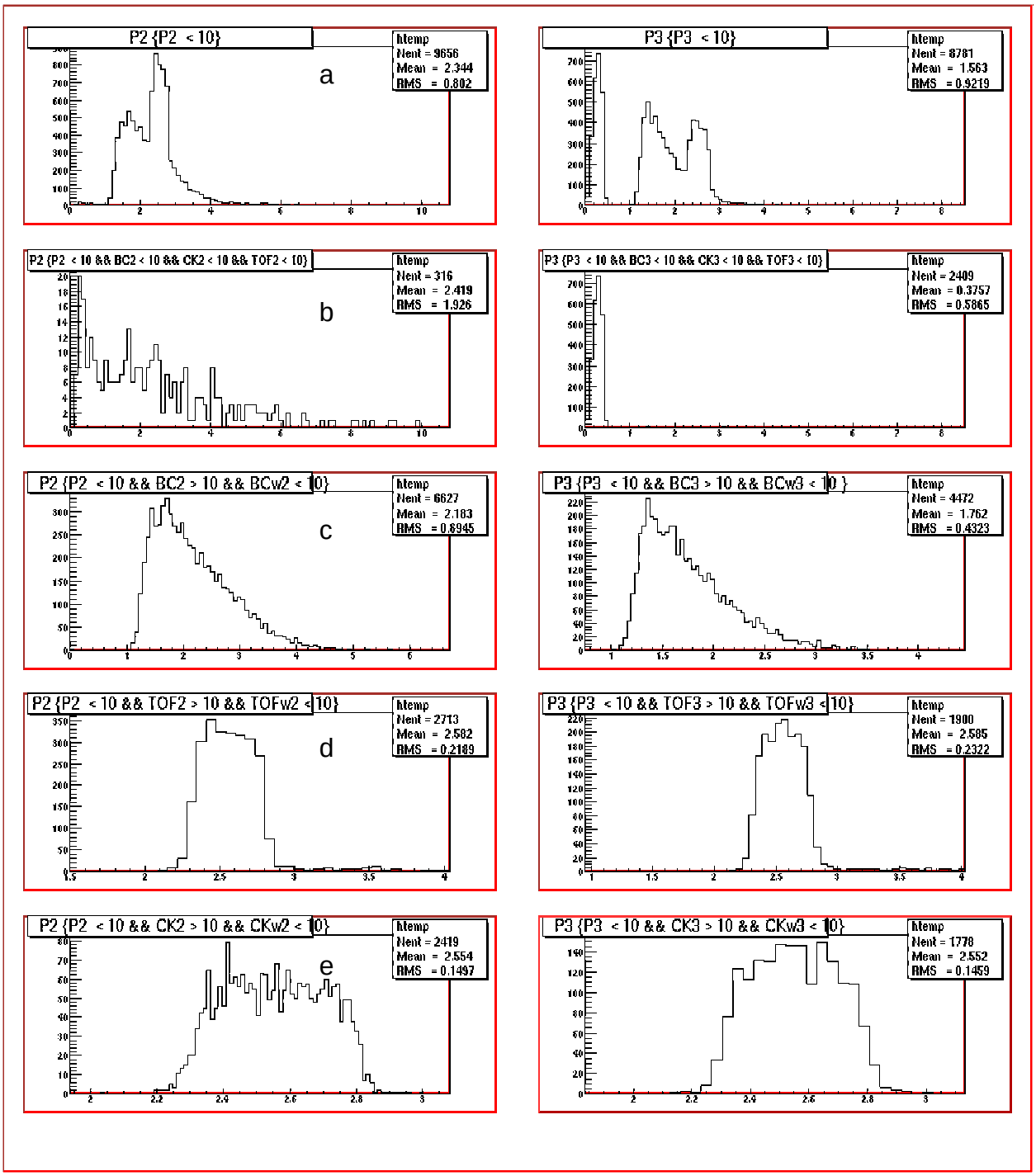

Fig. 2 - Kaon (left) and pion (right) momentum spectra for unrecoverable events having one ambiguous hit. The events are sorted by (a) all events, (b) events that missed BC, TOF, and CC, (c) events that hit BC but were unresolved, (d) events that hit the TOF but were unresolved, and (e) events which hit CC but were not identified (gas radiator).

Magnetic Simulation of the Hall D Spectrometer - Erratum

M. Lu and G.S. Adams

10 October 2000

This report corrects an error in the previous version of our magnet simulation report (05.06.2000) and shows the results for several modifications of the original LASS magnet geometry. In the previous report an error in the setup of the simulation code resulted in fringe fields that were too large.

A new 2D simulation of the Hall D spectrometer, including the LGD region, has been made. The purpose of the calculation was to obtain estimates of the fringe fields in the regions where detectors will be located. More precise 3D estimates will be carried out by P. Brindza as the spectrometer design evolves.

The calculation was carried out with the Flux2D code. An axially symmetric model of the spectrometer was constructed from Eric Scott's CAD drawing of 15 April. That drawing also forms the basis for the present monte carlo database. We take the coordinate system from that drawing also; the origin is located at the upstream edge of the steel endcap and the z axis is along the beam direction. Zero-field boundary conditions were set at z = -30m, z = +40m, and r = 40m. The materials used in the simulation were either 1010 steel or vacuum. The saturation properties of 1010 steel were interpolated by the code between an initial relative permeability of 3000 and a saturation field of 2.2 Tesla.

Four different geometries are shown here for comparison. In all cases the current was adjusted to produce a central field of 2.2 T. In the first case, the endcap was moved upstream to allow for cable access, but otherwise the magnet has the original LASS configuration (Fig.1). Field maps for this geometry are given in Table 1, and the field lines are shown in Fig.1. For the purposes of comparison one can approximate the radial positions of the Cherenkov and TOF photomultiplier tubes as 132 in and 54 in, respectively. A total of 6.4k grid elements were used in the calculation, and a driving current of 7.0 MA was used. As one can see from Table 1, the fringe fields in the Cherenkov and TOF regions are about 370 gauss and 990 gauss, respectively. While we have no solid numbers from LASS to compare with these, they are commensurate with the heavy magnetic shielding that was needed in that design. Lastly, the field in the region of LGD pmt shields is about 500 gauss, much to high for passive shielding on each tube to be effective without introducing large dead regions in the detector volume.

Table 1:

d (in)	**B_{axis} (Tesla)** **(r=0.1in, z=40in+d)**	**$B_{cerencov}$(Tesla)** **(z=212in, r=d)**	**B_{tof}(Tesla)** **(z=228in, r=d)**	**B_{lgd}(Tesla)** **(z=263in, r=d)**
0.0	2.18	0.31	0.14	0.043
6.0	2.09	0.17	0.10	0.054
12.0	2.12	0.17	0.11	0.050
18.0	2.11	0.16	0.10	0.051
24.0	2.10	0.15	0.098	0.050
30.0	2.09	0.13	0.095	0.049
36.0	2.05	0.12	0.089	0.047
42.0	2.21	0.11	0.086	0.046
48.0	2.12	0.10	0.081	0.044
54.0	2017	0.099	0.078	0.043
60.0	2.24	0.097	0.075	0.041
66.0	2.20	0.096	0.072	0.040

Table 1:

72.0	2.23	0.093	0.069	0.038
78.0	2.23	0.089	0.065	0.036
84.0	2.28	0.083	0.062	0.034
90.0	2.32	0.076	0.058	0.033
96.0	2.11	0.069	0.053	0.031
102.0	2.23	0.062	0.049	0.029
108.0	2.13	0.057	0.045	0.028
114.0	2.12	0.051	0.041	0.027
120.0	2.17	0.045	0.038	0.025
126.0	1.63	0.041	0.035	0.024
132.0	2.13	0.037	0.032	0.022
138.0	0.49	0.033	0.029	0.021

The need to reduce the fringe field below the values seen in LASS was already recognized in the early versions of our spectrometer design. The easiest way to reduce the fringe field is to fill the existing gaps in the steel yoke with more steel. These gaps will not be needed in our design. In our second case study these gaps were filled, and the driving current reduced to 6.8 MA to maintain the central field at 2.2 T. The results are shown in Fig. 2 and Table 2. This single modification produces a marked reduction in the fringe fields. The fields in the region of the Cherenkov and TOF detectors drop to 77 gauss and 250 gauss, respectively. The field in the region of the LGD is also reduced, but the resulting field of about 200 gauss is still rather high. It is not possible to predict the response of the individual LGD photomultiplier shields using the present 2D model because the LGD lacks the required axial symmetry.

Table 2:

d (in)	**B_{axis} (Tesla)** **(r=0.1in, z=40in+d)**	**$B_{cerencov}$(Tesla)** **(z=212in, r=d)**	**B_{tof}(Tesla)** **(z=228in, r=d)**	**B_{lgd}(Tesla)** **(z=263in, r=d)**
0.0	2.07	0.12	0.049	0.020
6.0	2.10	0.12	0.059	0.019
12.0	2.12	0.11	0.057	0.020
18.0	2.11	0.11	0.053	0.018
24.0	2.11	0.092	0.049	0.018
30.0	2.12	0.078	0.044	0.017
36.0	2.13	0.064	0.038	0.016
42.0	2.18	0.051	0.033	0.015
48.0	2.07	0.040	0.029	0.014
54.0	2.15	0.032	0.025	0.013
60.0	2.30	0.026	0.022	0.013
66.0	2.26	0.022	0.019	0.012
72.0	2.27	0.019	0.017	0.011
78.0	2.30	0.018	0.015	0.010
84.0	2.31	0.016	0.013	0.0093
90.0	2.30	0.015	0.013	0.0087
96.0	2.25	0.013	0.012	0.0081
102.0	2.12	0.012	0.011	0.0075
108.0	2.82	0.011	0.010	0.0070

Table 2:

114.0	3.10	0.010	0.089	0.0065
120.0	2.23	0.0092	0.082	0.0061
126.0	1.91	0.0084	0.0075	0.0057
132.0	1.54	0.0077	0.0070	0.0054
138.0	1.25	0.0071	0.0064	0.0050

Case 3 (Fig. 3 and Table 3) and Case 4 (Fig. 4 and Table 4) add a thin steel cylindrical shell around the LGD region to shield the individual shields that will be used on each photomultiplier. The shell thickness was arbitrarily set to 0.2 in, and the radius was set to 40 in. The cross sectional area of this shell is approximately equal to the area of the LGD. Case 3 adds this shield to the unmodified yoke geometry of Case 1. Case 4 adds this shield to the geometry having the gaps in the yoke filled. Case 4 represents our final result. A grid of 26k elements was used in the calculation and a driving current of 6.8 MA was used. In this case the yoke saturates in a small volume near the downstream bore hole but in the bulk of the yoke the field stays below 2.1 T. The field in the LGD shield goes into saturation in some regions so a thicker box would yield a lower internal field. However it is not clear yet if this is necessary. From Table 4 and Fig. 4 we observe that the fringe field in the regions of the Cherenkov, TOF and LGD detectors is predicted to be about 73 gauss, 220 gauss, and 110 gauss, respectively. These values fall within the range that can be effectively handled with passive shields.

The TOF detectors reside just upstream of the LGD shield. Because of their close proximity to large amounts of magnetic material they will experience a large B field which is hard to calculate accurately, both in magnitude and direction. To use passive shields one must pay careful attention to the direction of the field, and the mechanical stresses can be large. A safer approach may be to design the TOF counters with pmts that can withstand high magnetic fields. Published measurements have shown that good timing resolution can be achieved in this way.

In summary, by filling the gaps in the LASS magnet yoke and adding a passive shield around the LGD detector it is possible to dramatically reduce the expected fringe field in the regions where the Cherenkov, TOF, and LGD photomultipliers will be located. The expected fringe fields are sufficiently small that they can be effectively shielded by individual passive shields around each pmt.

Table 3:

d (in)	**B_{axis} (Tesla)** **(r=0.1in, z=40in+d)**	**$B_{cerencov}$(Tesla)** **(z=212in, r=d)**	**B_{tof}(Tesla)** **(z=228in, r=d)**	**B_{lgd}(Tesla)** **(z=263in, r=d)**
0.0	2.10	0.18	0.13	0.039
6.0	2.12	0.18	0.13	0.039
12.0	2.10	0.17	0.12	0.039
18.0	2.07	0.16	0.11	0.039
24.0	2.07	0.15	0.10	0.040
30.0	2.09	0.13	0.096	0.041
36.0	2.12	0.12	0.090	0.042
42.0	2.18	0.11	0.084	2.22
48.0	2.17	0.10	0.079	0.043
54.0	2.17	0.098	0.076	0.042
60.0	2.18	0.096	0.073	0.041
66.0	2.18	0.094	0.070	0.040
72.0	2.22	0.091	0.067	0.039

Table 3:

78.0	2.23	0.087	0.064	0.037
84.0	2.23	0.081	0.061	0.035
90.0	2.21	0.076	0.057	0.034
96.0	2.12	0.069	0.053	0.032
102.0	2.05	0.062	0.049	0.030
108.0	2.23	0.056	0.048	0.029
114.0	1.83	0.050	0.041	0.027
120.0	1.54	0.045	0.038	0.025
126.0	1.11	0.040	0.034	0.024
132.0	0.72	0.036	0.031	0.022
138.0	0.71	0.033	0.029	0.021

Table 4:

d (in)	**B_{axis} (Tesla)** **(r=0.1in, z=40in+d)**	**$B_{cerencov}$(Tesla)** **(z=212in, r=d)**	**B_{tof}(Tesla)** **(z=228in, r=d)**	**B_{lgd}(Tesla)** **(z=263in, r=d)**
0.0	2.07	0.14	0.075	0.011
6.0	2.09	0.13	0.072	0.011
12.0	2.07	0.12	0.067	0.011
18.0	2.07	0.11	0.060	0.010
24.0	2.07	0.093	0.052	0.0096
30.0	2.05	0.077	0.044	0.0087
36.0	2.11	0.062	0.037	0.0084
42.0	2.14	0.049	0.030	2.09
48.0	2.17	0.038	0.025	0.011
54.0	2.23	0.030	0.022	0.012
60.0	2.23	0.024	0.019	0.011
66.0	2.23	0.021	0.017	0.011
72.0	2.27	0.018	0.015	0.010
78.0	2.27	0.016	0.014	0.0095
84.0	2.28	0.015	0.013	0.0088
90.0	2.24	0.014	0.012	0.0083
96.0	2.27	0.012	0.011	0.0077
102.0	2.06	0.011	0.0098	0.0072
108.0	2.19	0.010	0.0091	0.0067
114.0	1.89	0.0094	0.0084	0.0063
120.0	1.82	0.0086	0.0077	0.0059
126.0	0.99	0.0079	0.0071	0.0055
132.0	0.96	0.0073	0.0066	0.0052
138.0	0.73	0.0067	0.0061	0.0048

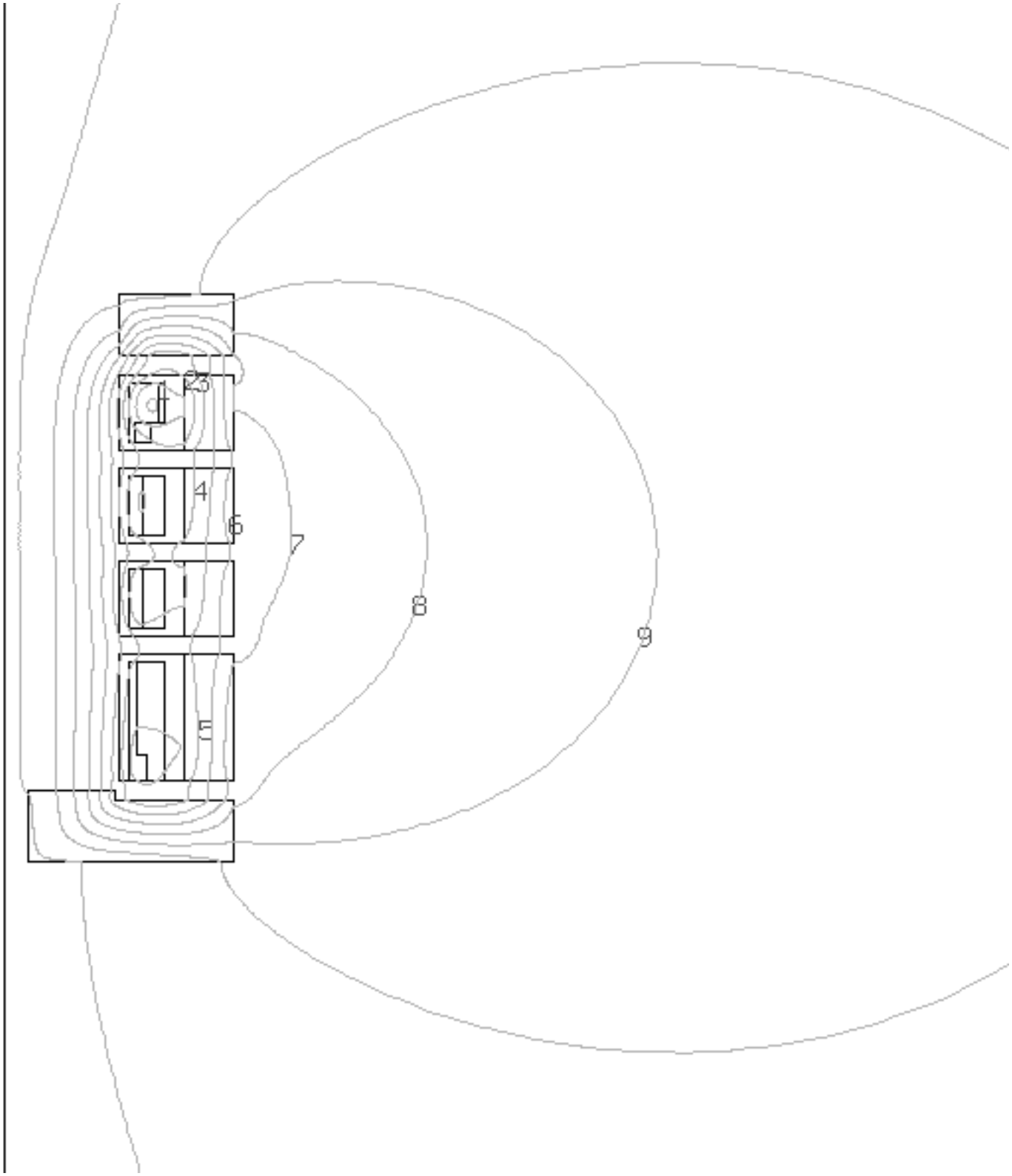

Fig. 1 - Case 1 geometry and field.

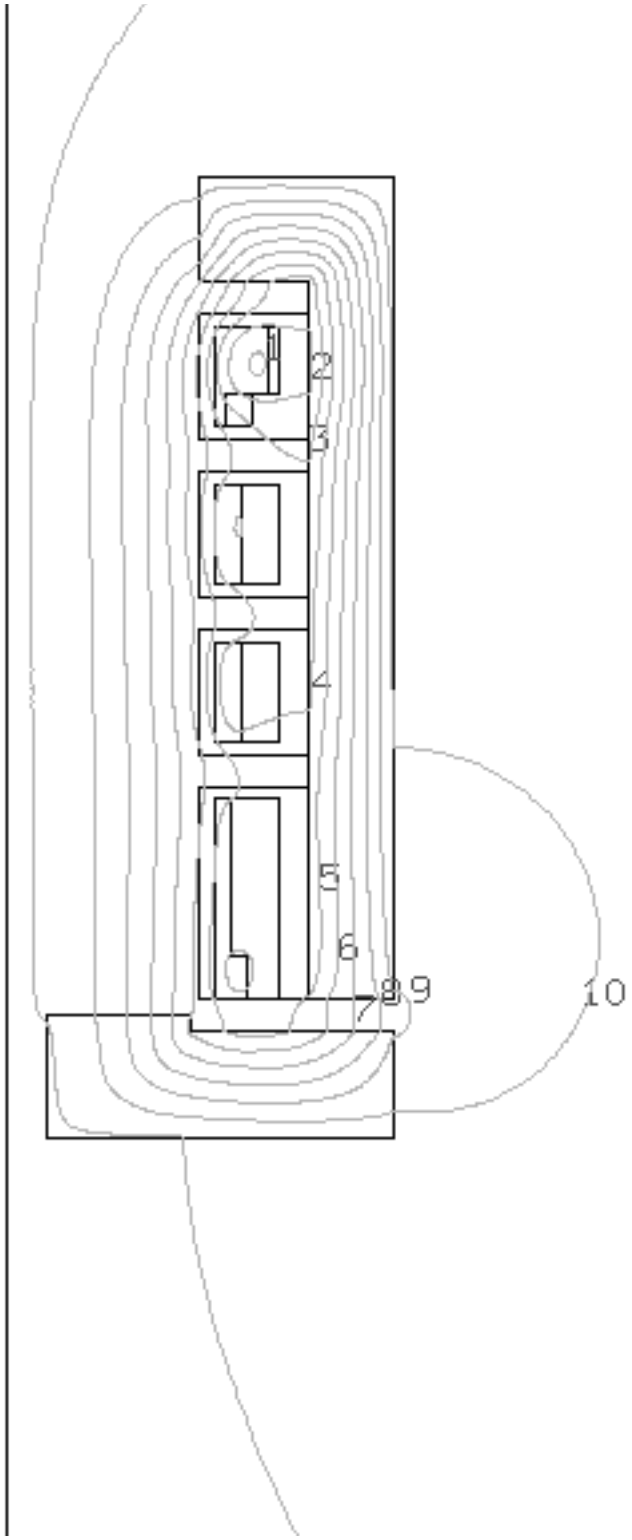

Fig. 2 - Case 2 geometry and field.

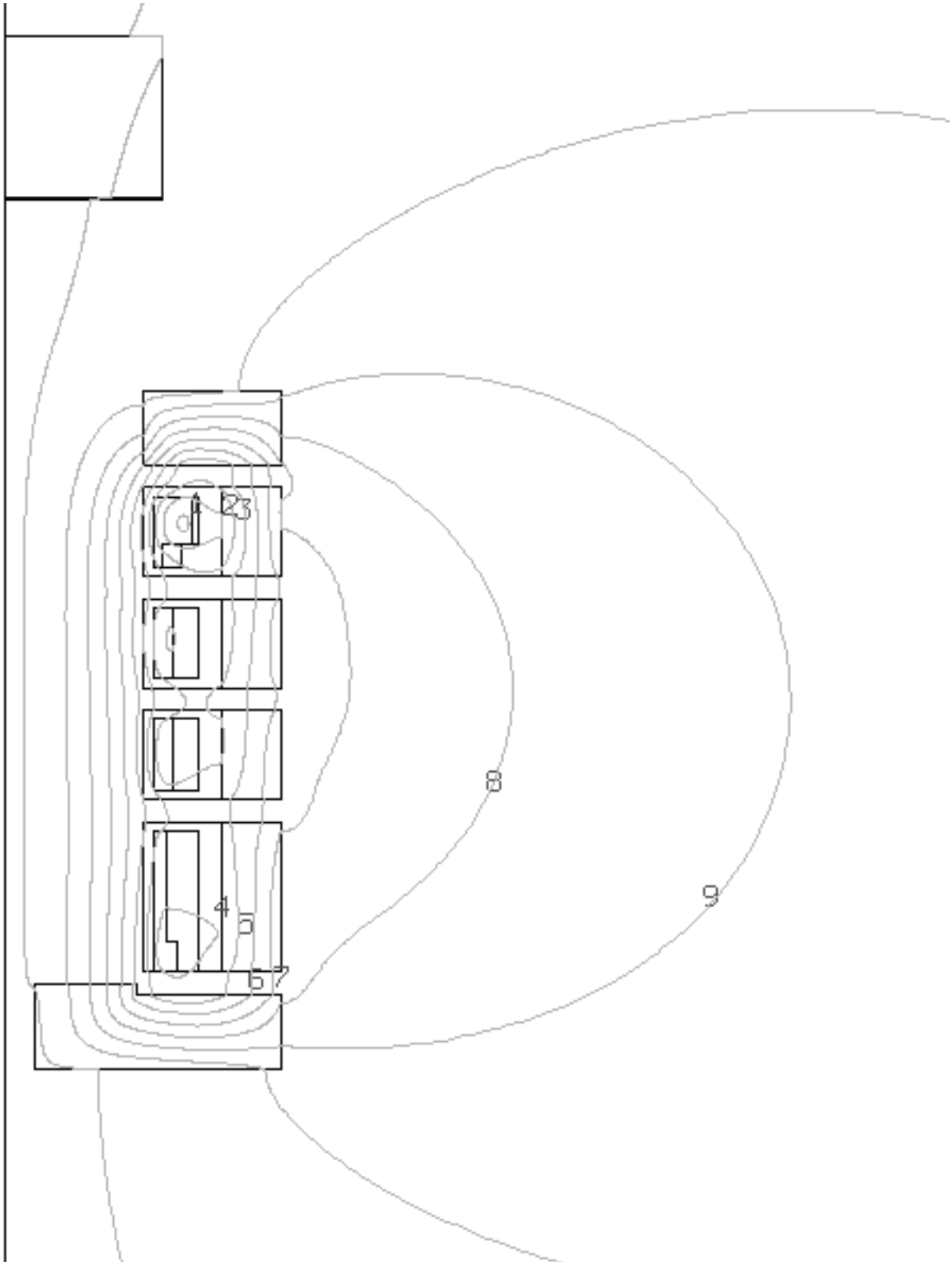

Fig. 3 - Case 3 geometry and field.

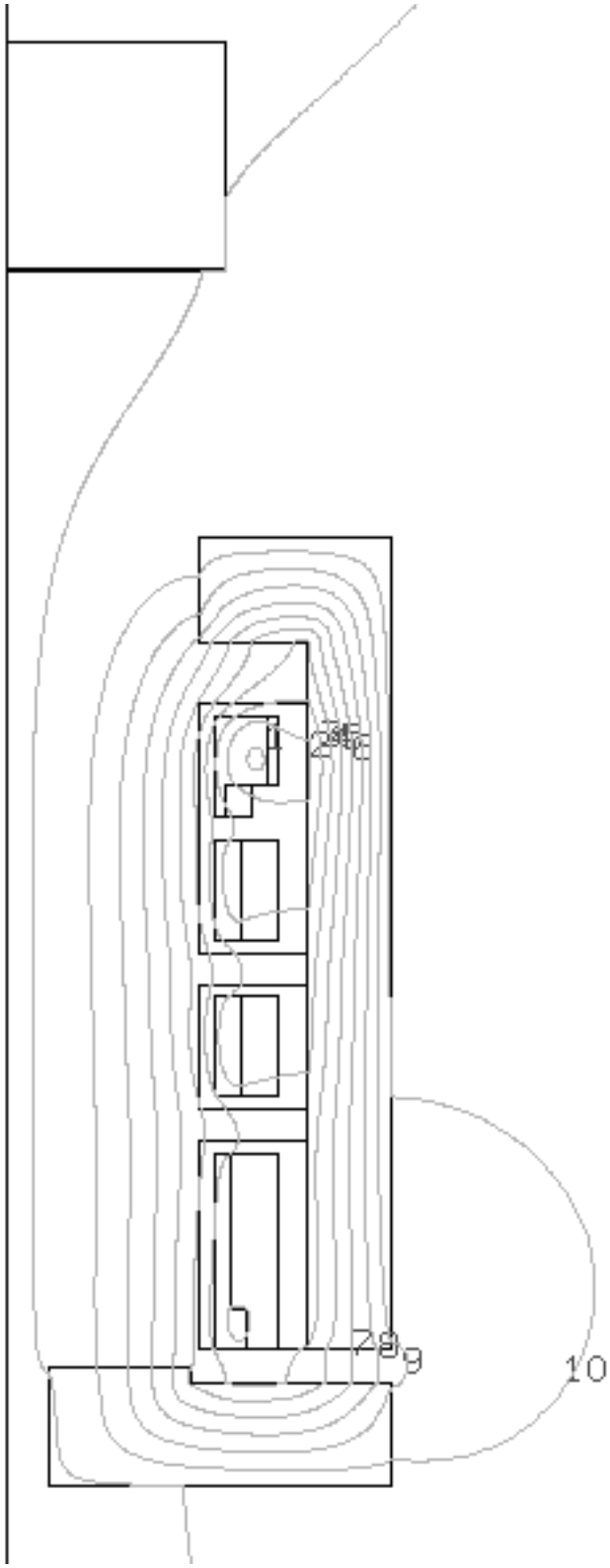

Fig. 4 - Case 4 geometry and field; final result.

Status of the Hall-D Particle Identification System

Gary Adams and Richard Heinz
1 November 2001

Introduction

One of the crucial issues in the Hall D detector design is the development of a technique to measure particle velocities, necessary for charged particle identification. This report presents the anticipated performance of the three relevant Hall D subsystems, the Cherenkov detector, the downstream time-of-flight (TOF) scintillators, and the TOF signals from the barrel calorimeter. These three systems will be used to discriminate between species of charged particles. The proposed particle identification system will discriminate between pions, kaons, and protons. Because the R&D for these subsystems is ongoing, there is of necessity some uncertainty in the results that we present. For each subsystem we discuss performance assumptions and some of the important aspects that we will be studying.

Cherenkov Subsystem

It is not possible to use TOF alone to achieve the desired level of particle discrimination unless one were to design extremely long flight paths. This conflicts with the goal of achieving large angular coverage in the spectrometer. Therefore a threshold Cherenkov detector will be used to determine the speed of high momentum tracks [1]. The radiator material was chosen to be C_4F_{10} because it offers the lowest threshold speed for an environmentally friendly gas. At atmospheric pressure this radiator has an index of refraction equal to 1.0053. This allows one to make a positive identification of pions up to about 8 GeV/c in momentum.

The current optics design is shown in Fig. 1. The detector is sectioned into sixteen identical azimuthal segments. The segments are not optically isolated. This was done to maximize the light collected for near-threshold pions. Because those tracks have a small Cherenkov angle, they will deposit all of their light in one sector, even if the track crosses a sector boundary.

Cherenkov light is piped out of the radiator volume and onto the PMT face (Burle 8854) by reflection on two mirrors. The advantage of this design is that the PMT can be moved to the downstream side of the Cherenkov box, where the fringe field is lower [2]. Also the added freedom of a second reflection allows us to place the PMT axis perpendicular to the direction of the magnetic field. This is the optimum angle for magnetic shielding. A prototype shield for the PMTs has been purchased and we expect to start testing it within a month. This shield is constructed from four cylindrical layers of high-permeability metals all on a common axis. The opening to the PMT is tapered to match the solid-angle of photons leaving the second stage mirror and entering the PMT face. The present optics require an opening angle of about ± 22 degrees. Since the first stage mirrors lie in the flight path of the TOF and LGD detectors it is necessary to minimize the amount of material that particles traverse in the mirror. These mirrors will be con-

structed from vinyl foam surrounded by carbon fiber fabric impregnated with epoxy. The mirror surface is Aluminum on Lexan with a protective coating of SiO_2.

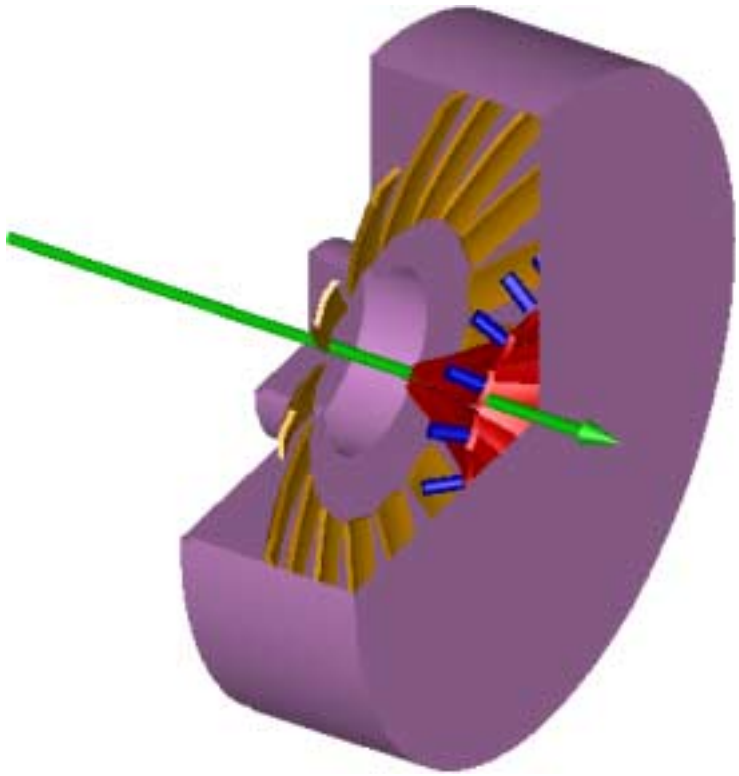

Fig. 1 - Sectioned view of the Cherenkov design.

The performance of the optics was tested with a Monte Carlo simulation. The Hall D Monte Carlo code was used to generate $K^+K^-\pi^+\pi^-$ events and transport them through the solenoid and Cherenkov detector. Photons were generated according to the velocity of the particles and randomly distributed in azimuthal angle [1]. The number of photons was attenuated by the known reflectivity of Aluminum as a function of wave length. Finally, photoelectrons were produced in the photocathode of the PMT (Burle 8854) according to the known quantum efficiency of the PMT as a function of wave length. Attenuation in the gas radiator was not included because it is negligible for high purity gas.

Fig. 2 summarizes the performance of the new optical design for tracks that hit a single first-stage mirror. The distribution of photons on the face of the PMT is shown in a scatter plot. The red points are for the central mirror sector and the blue and green points are for the PMTs in the adjacent sectors. The points at small values of X (left side of graph) are located closer to the beam axis. This figure shows that the assumed detector segmentation is nearly optimum for the

reaction of interest. Cross talk between the sectors is small for large angle pions and large for small angle pions. It also shows that a five inch pmt is adequate for this design.

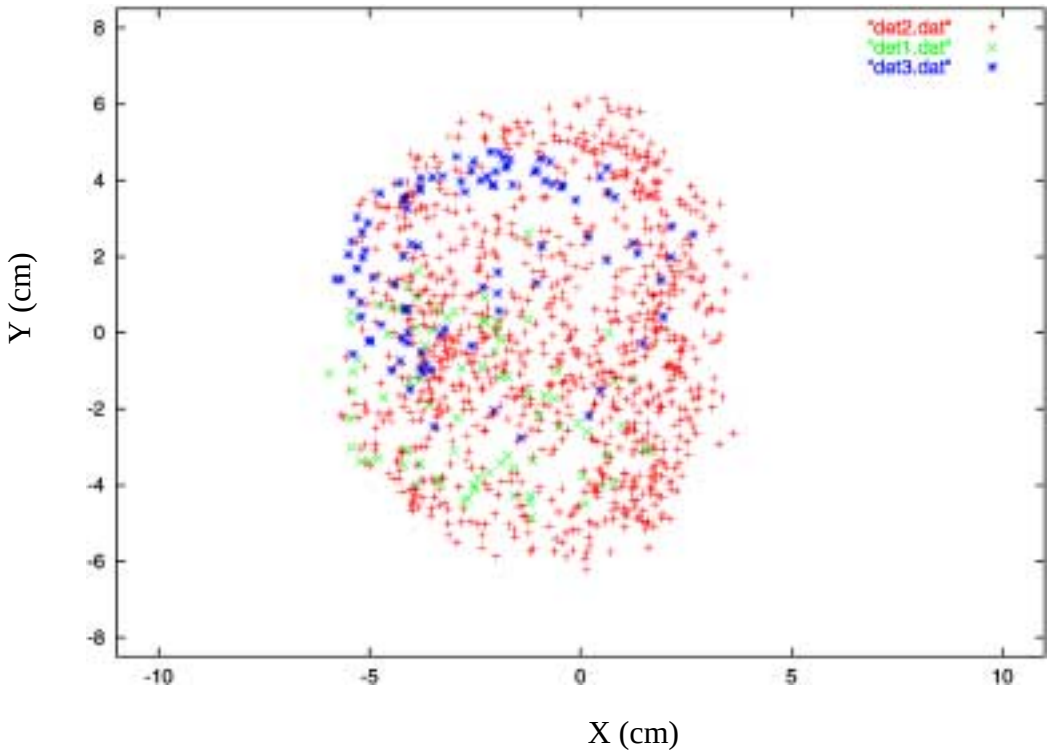

Fig. 2 - Photon distribution on the Cherenkov pmt face.

The pion detection efficiency as a function of momentum is plotted in Fig. 3 for two values of the detection threshold. The solid histogram is for a one-photoelectron threshold, and the dashed line is for a two-photoelectron threshold. These results are consistent with our earlier esti-

mates of the detection threshold [3]. They show that efficient pion identification can be made for momenta greater than about 2.9 GeV/c.

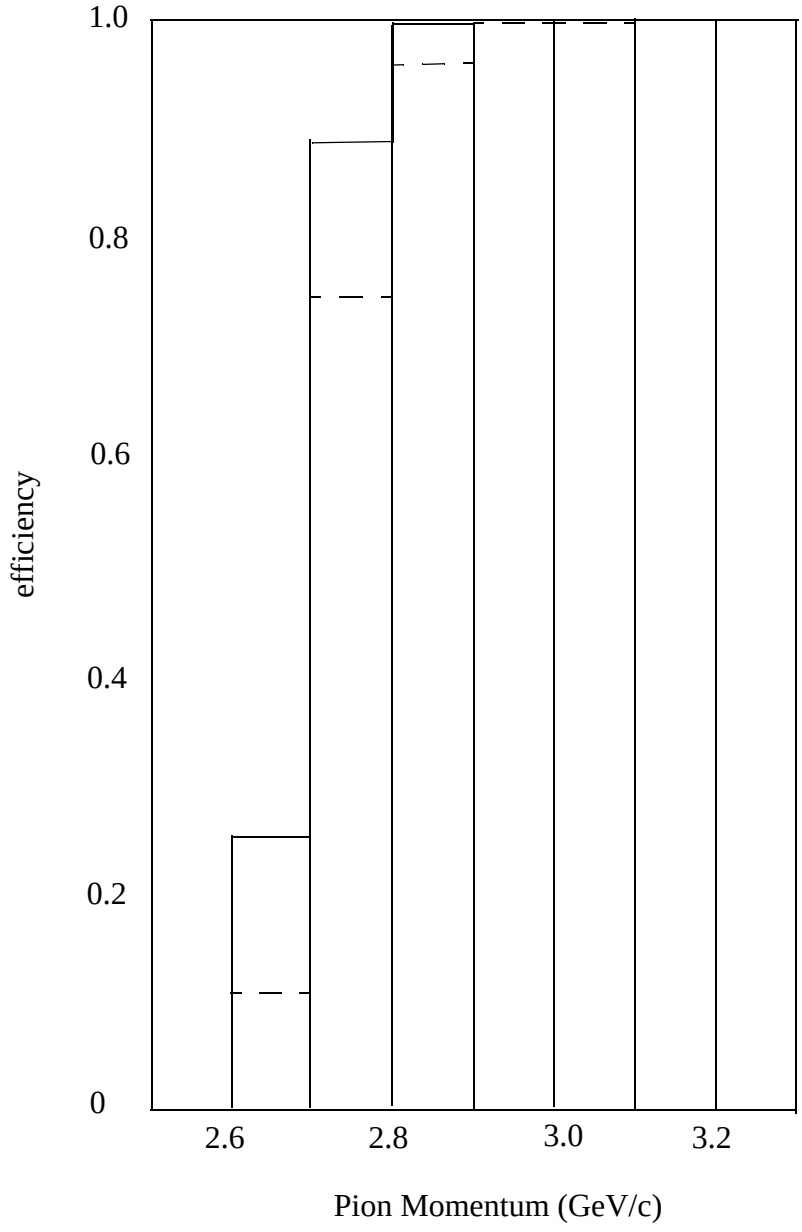

Fig. 3 - Pion detection efficiency of the Cherenkov detector.

Knock-on electrons produced by kaon interactions can result in kaons being incorectly identified as pions in the Cherenkov detector. The rate of these misidentifications will be calculated at a later time when the amount of material in front of the Cherenkov detector is better known. Based on the results of a similar detector now being used in the CLAS spectrometer one can make an order of magnitude estimate; the misidentification rate will be less than one percent of the kaon rate. Also, further simulations are needed to determine the optimum segmentation of the Cherenkov detector.

We have started to address some of the engineering issues related to the Cherenkov detector. Most of our current optical design has been incorporated into the Hall D IDEAS CAD program (Fig.1). After further refinement this design will be integrated into the Hall-D Design Report. The current detector design is more compact than the original single-mirror design. This may allow us to assemble major components of the detector off site. It is also our intention to move the design into the GEANT simulation package for Hall D.

Downstream TOF Subsystem

The TOF subsystem is composed of two walls of scintillator. Each wall is 2 m by 2 m and is formed by scintillator bars each 2 m long. The bars are horizontal in one wall, vertical in the other. At IHEP we tested bars with 2.5 cm and 5.0 cm square cross sections. We measured the time resolution as a function of the entry point of the beam particle along the 2 m dimension of the bars. Fig. 4 shows results for the two bars tested. The ordinate is the bar time resolution in picoseconds, while the abscissa indicates the entry position (along the 2.0 m bar dimension) of the beam.

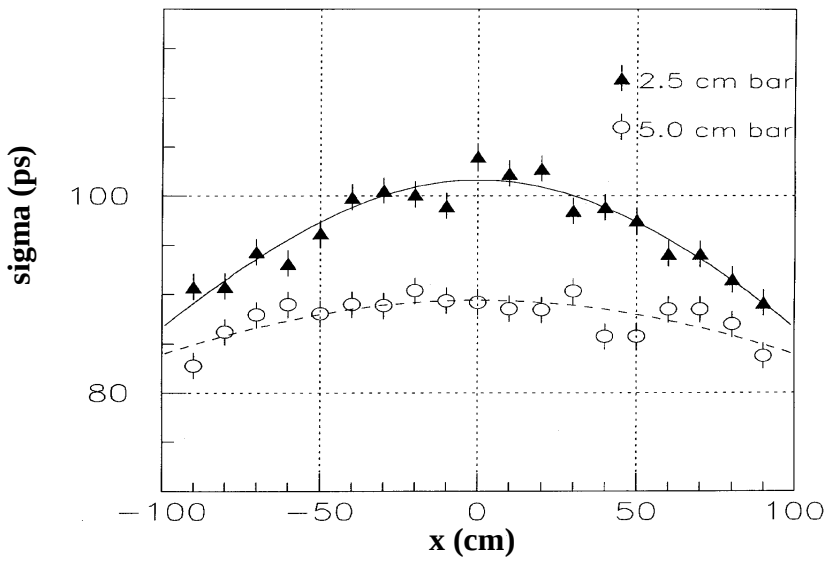

Fig. 4 - Time resolution versus entry position for the downstream TOF detectors.

Since there is a phototube (XP2020) on each end of the bar, the time resolution is worse at the center of the bar, where less total light is collected. (The effective attenuation length is about 1.4 m for the smaller bar and 2.5 m for the larger bar.) Based on these results (and granularity studies of the physics), we are planning on using 5.0 cm square bars for Hall D. The above figure shows that we will have a time resolution of 83 ps to 90 ps. The results in the above figure are an upper limit, since they do not correct for the finite size of the trigger counters, an effect of about 10%. Thus we are confident that we can achieve a resolution of 80 ps or less in the center of a 5.0 cm bar. Since there are two TOF planes, this gives an overall TOF resolution of 57 ps for the very

center of the TOF detector (if one neglects correlated errors such as the error in the common start time), better near the edges.

We are lead by the above results to state a design goal of 80 ps for the TOF subsystem. (We thus do not depend on getting signals from both planes, which would give a better resolution.) The probability of identifying a pion in the downstream TOF detector is shown in Figure 5. Here we applied the criterion that a pion is identified if its measured time-of-flight is closer to that expected from a pion than that expected from a kaon. Besides the 80 ps results (middle curve) we show the pion detection probability for 60 ps (top curve) and 100 ps (bottom curve). A comparison with Figure 3 shows how the Cerenkov and TOF subsystems complement each other. At 2.5 GeV/c, below the Cerenkov threshold for pions, the TOF is 99%, 97%, or 93% efficient at 60 ps, 80 ps, and 100 ps resolutions respectively. By 3 GeV/c the Cerenkov is essentially 100% efficient and the TOF is still over 85% efficient even for 100 ps resolution and over 90% efficient for 80 ps or better resolution.

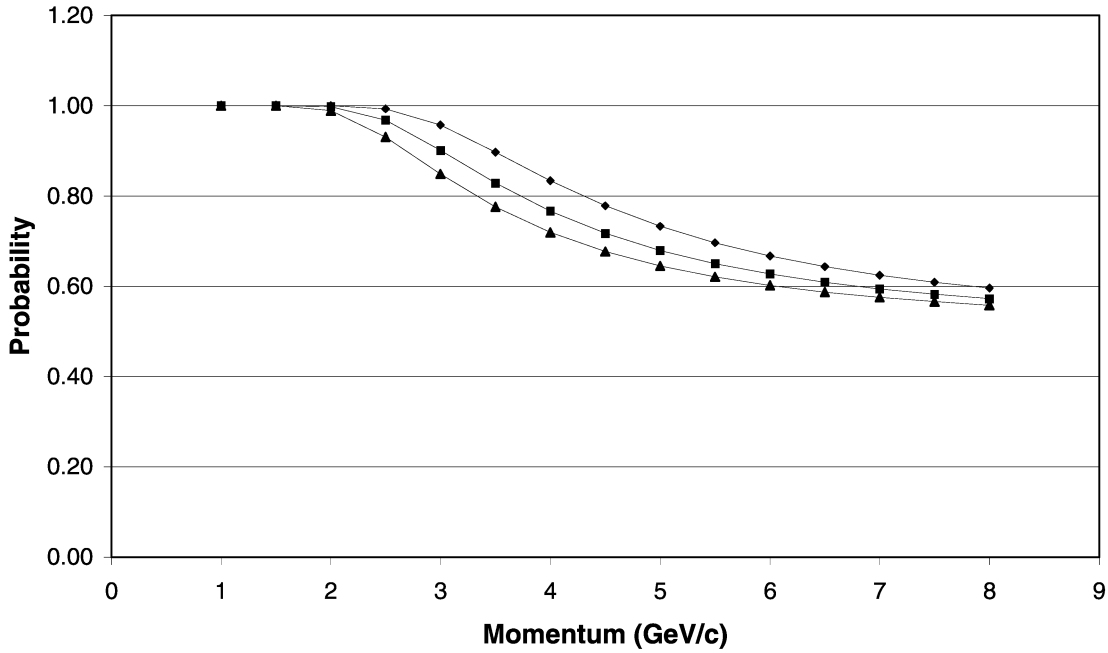

Fig. 5 - Probability of identifying a pion in the downstream TOF. The top, middle, and bottom curves are for resolutions of 60ps, 80ps, and 100ps, respectively.

There are many factors that could alter the time resolution, but these should, taken together, lead to a resolution of 80 ps or somewhat less. We list these items in categories of Diminished and Improved resolution effects.

Diminished:

1. Mass production of a subsystem consisting of many elements inevitably results in a poorer performance than that obtained in a bench test of a single element. Thus an element of the 160-element TOF walls (80 in each wall) will not achieve the resolution obtained by a single element in a test beam under ideal conditions.

2. A light pipe must be inserted between the scintillator and the PM, resulting in a loss of light.
3. We assume a perfect time resolution for the TOF common start. If the start counter can identify the RF bucket involved in the interaction, the hardware common start time can probably be corrected to less than 10 ps, which is negligible.

Improved:

1. As mentioned above there will be two scintillator walls in the TOF, and each wall will give an independent time measurement. Exceptions occur when a particle goes through a crack or through the beam hole in one of the walls.
2. At IHEP the PMTs were butted up against the scintillator, losing light relative to the final subsystem arrangement of adhesive bonding.
3. At IHEP the beam entered the scintillator normally; at Hall D the beam will in general pass through at an angle, generating more light.
4. At IHEP the 5cm by 5cm scintillator bar butted up against the 5cm diameter PM. We will see if tapering our light down to a 3.3cm circle will improve resolution by directing light onto the sweet spot of the PMT.
5. Cosmic Ray and IHEP results have shown that the TOF is sensitive to the type of constant fraction discriminator (CFD) used. We will search for a better CFD.
6. Glass may be substituted for scintillator, so that the light is prompt Cherenkov light instead of time-delayed light from fluor excitation. Also, a phototube with better time resolution could be used – an XP 2020/UR instead of an XP2020.

Barrel Calorimeter

The present design for the barrel calorimeter incorporates TOF measurements derived from timing signals measured at both ends of the Pb/Scifi bars. Based on the measured performance of similar detectors in the KLOE experiment [4] one can expect a TOF resolution of about 250 ps in our detector. While this resolution is much wider than the value expected for the downstream TOF detectors it is still a useful component of the PID system because it covers a large part of the total solid angle for charged tracks.

PID Performance

The overall performance of the PID system was estimated in a Monte Carlo simulation [2]. Useful information can also be found in earlier reports [5] that predate the final design. Ref. [2] also predates the final design but the detector parameters are very close to those described above.

In ref. [2] the HDFAST code was used to simulate the response of each of the above subsystems assuming a 9 GeV photon beam produces a single meson resonance at a mass of 2.0 GeV. The decay channel was $K^+K^-\pi^+\pi^-$. The assumed TOF resolution was 80 ps for the downstream TOF and 250 ps for the barrel calorimeter. In order to be identified by TOF the calculated difference in TOF between a pion and kaon of equal momenta was required to be less than three times the resolution of the detector at the measured momentum. This three-sigma limit will suppress pion contamination in the kaon signal by about a factor of 25.

A hard pion threshold at 2.8 GeV/c was assumed for the Cherenkov threshold. This value is slightly lower than the data in Fig. 3 would suggest. This difference is not sufficient to alter our previous conclusions.

The fraction of events that are completely determined by the PID system is only 26 percent, or about 70 percent per track. This simulation did not include any segmentation of the detectors. Therefore the low fraction of completely measured events is due to the fact that both the downstream TOF and the Cherenkov detectors span a limited angular range, and also because a rather stringent TOF requirement has been applied. However by imposing strangeness conservation one can relax the detector requirements to three resolved particles and then the event identificaton rate increases to 69 percent. Further improvements can be realized by making a kinematic fit on the remaining ambiguous tracks. The large mass difference between kaons and pions makes this a useful addition to the PID process. An overall event identification rate of 88 percent can be expected for $K^+K^-\pi^+\pi^-$ events. Although the details of the PID system remain to be worked out it is clear that the proposed combination of TOF and Cherenkov detectors will provide a good PID system for Hall D.

References

[1] See formulas 24.3 and 24.5 in The European Physical Journal C15, 2000.

[2] M. Lu and G.S. Adams, “Magnetic Simulation of the Hall D Spectrometer - Erratum,” Hall D Note no. 42.

[3] M. Belis, G. Adams and J. Cummings, “PID Acceptance Using TOF, Cherenkov and Kinematic Fitting,” Hall D Note no. 38.

[4] A. Antonelli, et al., Nucl. Inst. Meth. A354, 352 (1995).

[5] Curtis Meyer and Paul Eugenio, “A Study of combined K pi separation using time of flight and a gas Cherenkov detector,” Hall D Note no. 15; Paul Eugenio, “A study of acceptance for the Stage 1 Hall D Detector,” Hall D Note no. 16.